URBAN FINESCALE FORECASTING REVEALS WEATHER CONDITIONS WITH UNPRECEDENTED DETAIL

R. J. Ronda, G. J. Steeneveld, B. G. Heusinkveld, J. J. Attema, and A. A. M. Holtslag

Feasibility of numerical weather prediction at urban neighborhood and street scales is demonstrated for summer conditions in Amsterdam.

As the number of urban dwellers increases from an estimated 4 billion in 2014 to an expected 6.5 billion by 2050 (United Nations 2014), urbanization is putting an increasing strain on human comfort, productivity, and health in cities worldwide.

AFFILIATIONS: Ronda,* Steeneveld, Heusinkveld, and Holtslag—Meteorology and Air Quality Section, Wageningen University, Wageningen, Netherlands; Attema—Meteorology and Air Quality Section, Wageningen University, Wageningen, and Netherlands eScience Center, Amsterdam, Netherlands
*** ADDITIONAL AFFILIATION:** Ronda—Royal Netherlands Meteorological Institute, De Bilt, Netherlands
CORRESPONDING AUTHOR: R. J. Ronda, reinderronda@gmail.com

The abstract for this article can be found in this issue, following the table of contents.
DOI:10.1175/BAMS-D-16-0297.1

A supplement to this article is available online (10.1175/BAMS-D-16-0297.2).

In final form 17 March 2017
©2017 American Meteorological Society
For information regarding reuse of this content and general copyright information, consult the AMS Copyright Policy.

From a meteorological perspective, cities often experience an urban heat island (UHI) effect (Howard 1833; Oke 1982). This implies that urban dwellers are more vulnerable to the adverse effects of extreme heat, which is an issue of increasing relevance since the occurrence, severity, and duration of heat waves are expected to increase in the coming decades (IPCC 2013). Some of the adverse effects of extreme heat include diminished labor productivity (Zander et al. 2015), increased energy demand (Fazeli et al. 2016), and considerably higher risks of cardiovascular diseases, cancers, and respiratory diseases. These effects contribute to the increased mortality rate observed when temperatures exceed impact thresholds, which are climate-region dependent, above which human well-being and health deteriorate (Huynen et al. 2001; Curriero et al. 2002; Pirard et al. 2005).

Nowadays, in order to mitigate these adverse effects, urban design includes interventions that improve human thermal comfort and health (U.S. Environmental Protection Agency 2008; Rydin et al. 2012). Protecting people during heat waves relies on early warning systems (Kovats and Bickler 2012; McGregor 2015), which in turn depend on accurate weather forecasts (Pappenberger et al. 2015). Identified as "a quiet

revolution" by Bauer et al. (2015), the progress made in numerical weather prediction (NWP) has led to the development of systems that forecast operationally high-impact weather events up to about 1–2 weeks ahead of time on regional spatial scales ranging from a few kilometers to a few dozen kilometers.

Moving beyond the regional scale, we developed an urban weather forecasting system (UFS) that enables weather forecasts at the neighborhood and street scale. This is an important step forward in NWP since it is at these scales that people consume, sleep, work, and recreate. Forecasts at this level provide information that is directly relevant to the personal safety and well-being of people, while spatially distributed forecasts on these scales provide guidance important to health impact mitigation. Thus, governmental bodies, city planners, public health authorities, energy companies, citizens, and entrepreneurs can directly employ the forecasts produced by the UFS to direct their operations and influence their choices.

To test its applicability in finescale weather forecasting, we used the UFS during the summer months [June–August (JJA)] of 2015 to produce a daily weather forecast for Amsterdam, the capital city of the Netherlands (Fig. 1). Each day, a forecast was begun at 0000 UTC and was used to forecast the weather up to 48 h ahead. The flat Amsterdam metropolitan region has approximately 1 million inhabitants and lies about 3 m below sea level. Particularly noteworthy about the geography of the Amsterdam metropolitan region is the abundance of water in the form of shallow lakes, rivers, and hand-dug canals.

URBAN FINESCALE WEATHER FORECASTING SYSTEM. The UFS is based on version 3.5.1 of the Advanced Research core of the Weather Research and Forecasting (WRF) urban modeling system (Skamarock and Klemp 2008; Chen et al. 2011). Forecasts are produced on four one-way nested computational domains [Table 1 and Fig. ES1 in the

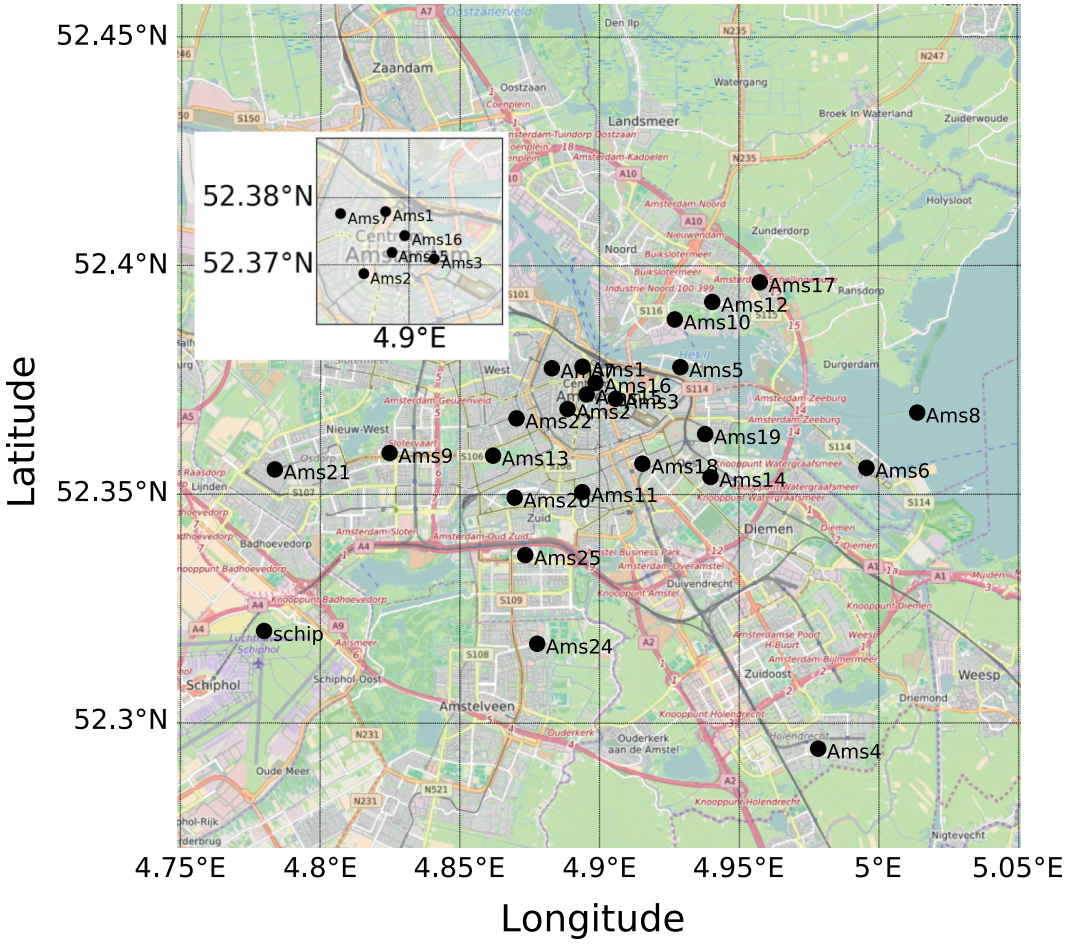

Fig. 1. OpenStreetMap (www.openstreetmap.org/#map=11/52.3525/4.8584) image of the city of Amsterdam and its surrounding areas showing the locations of the 24 weather stations and the location of the SYNOP Schiphol Airport weather station (WMO code 06240). The inset figure shows an enlargement of the map including the stations for the center of Amsterdam.

Table 1. Specification of the WRF computational domains.						
Domain identification	North–south extent (km)	East–west extent (km)	Grid spacing (m)	Central lat (°N)	Central lon (°E)	Time step (s)
d01	1,487.5	1,487.5	12,500	51.964	5.663	60
d02	300	300	2,500	52.374	4.820	12
d03	60	60	500	52.351	4.896	2.4
d04	17.5	13.5	100	52.352	4.907	0.48

supplemental material (available online at https://doi.org/10.1175/BAMS-D-16-0297.2)], the finest of which comprises the Amsterdam metropolitan region. This domain has a horizontal grid spacing of 100 m. The coarsest domain has a grid spacing of 12.5 km and comprises a major part of northwestern Europe. In total, the UFS employs 61 vertical terrain-following (eta) layers (Table ES1 in the supplemental material) from the surface up to a pressure level of 50 hPa.

For grid cells whose land use is categorized as urban, the exchange between the land surface and the lower atmosphere is calculated using the single-layer urban canopy model (SLUCM) (Kusaka et al. 2001). This model uses the empirical formulation of Narita (2007) for determining the transfer of energy from the walls of the buildings and the road up toward the canopy. SLUCM is also used to integrate the prognostic variables associated with the energetic state of the urban fabric including the temperatures of the materials that make up the roofs and walls of the buildings, as well as the temperatures of the road materials.

The development of the UFS consisted of three steps (Fig. 2). The first step is the geographic information preparation step, which consisted of processing innovative data resources on topographic element mapping, aerial photography, and laser altimetry. These were used to determine land use, soil type, surface impermeability, and urban morphological characteristics (Ching et al.

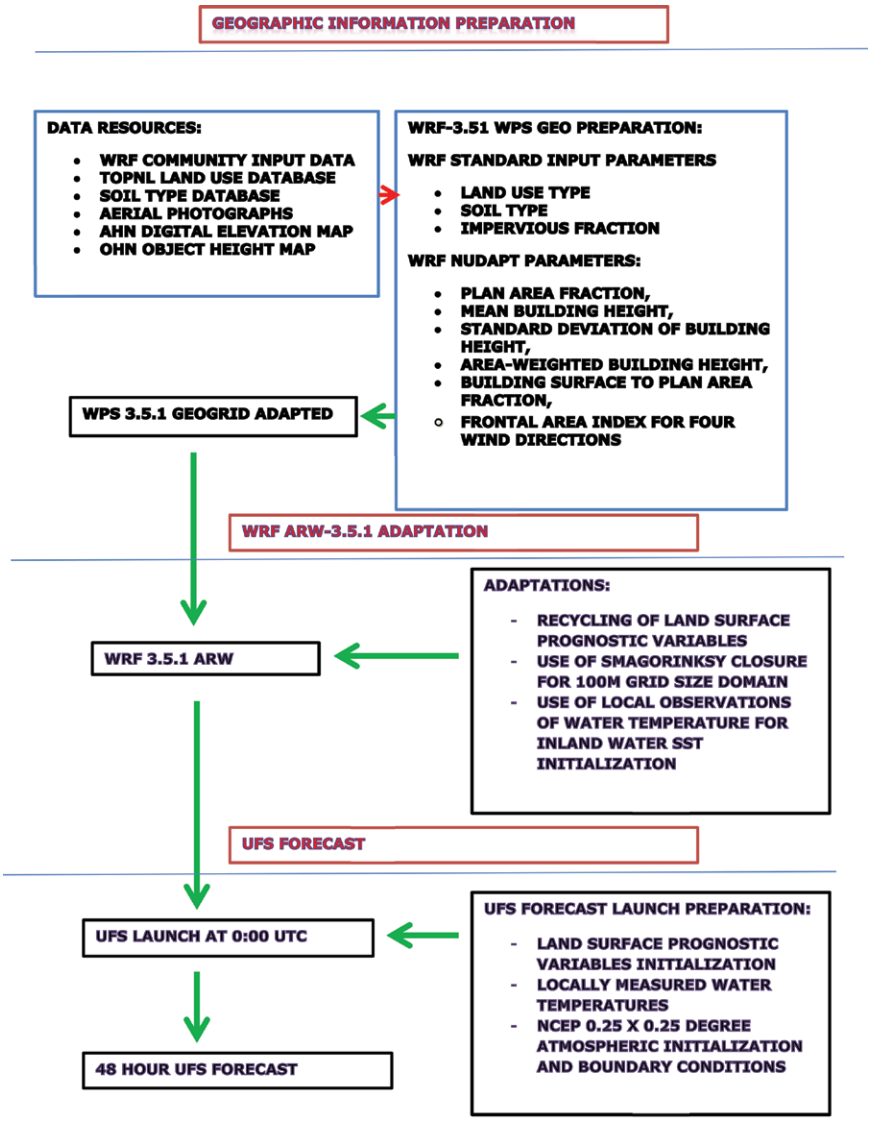

Fig. 2. Flow diagram of the UFS describing the steps that were needed to successfully produce forecasts for the Amsterdam metropolitan region.

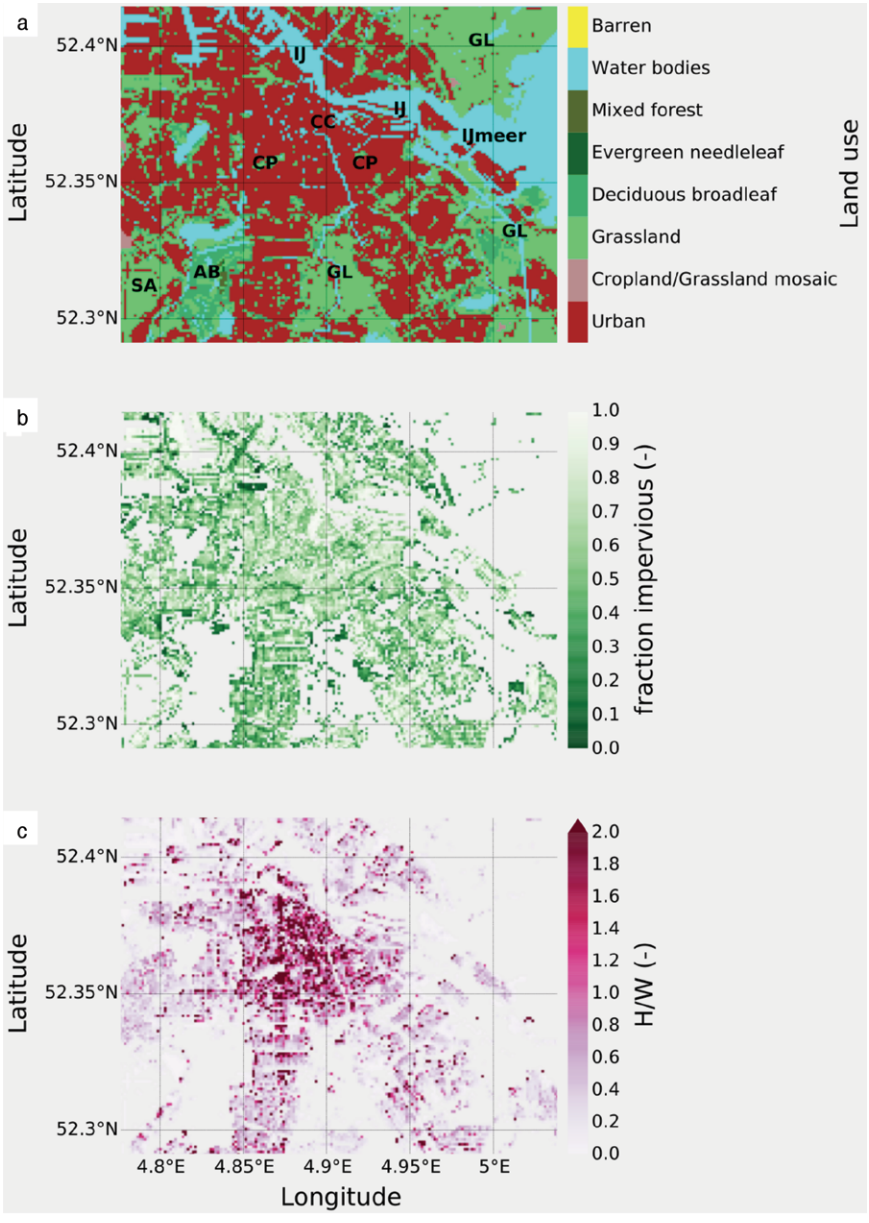

Fig. 3. Specification of land-use and urban morphological characteristics. (a) Land use for all grid points of the smallest domain. Labels denote the geographical location of the city center (CC), the major water bodies (IJ and IJmeer), grasslands (GL), the major city parks (CP), Amsterdamse Bos (AB), and Schiphol Airport (SA). (b) Impervious (nonvegetated) fraction and (c) aspect ratio for all grid points in the smallest domain for which land use is classified as urban.

2009), which were subsequently applied to generate geographical data files within the WRF preprocessing system (WPS).

The second step is the WRF adaptation step. In this step, we extended WRF to enable the initialization of soil and urban fabric prognostic variables from previous forecasts. We also extended WRF to allow the specification of inland water temperatures (lakes, ponds, rivers, and canals) for the two finest computational grids from a local measurement network of water temperatures operated by Rijkswaterstaat, the Dutch agency responsible for the management of the main (water) infrastructure in the Netherlands. Furthermore, we adapted WRF such that for all vertical layers within the finest computational grid, turbulent diffusion is calculated with the Smagorinsky first-order closure [three-dimensional (3D)] option. With this methodology, only subgrid-scale turbulence diffusion is accounted for, while the largest (flux carrying) eddies are expected to be resolved explicitly by the modeling system (Talbot et al. 2012). For the coarser computational grids, vertical turbulent diffusion is parameterized according to the Yonsei University (YSU) planetary boundary layer (PBL) scheme (Hong et al. 2006), while horizontal turbulent diffusion is accounted for by the standard Smagorinsky first-order closure [two dimensional (2D)].

Steps 1 and 2 conclude the development of the UFS, which is now ready to be used to produce forecasts for the urban area of Amsterdam. Details, including a full description of the employed land-use datasets, as well as computer codes, scripts, and configuration files, are available as a GitBook repository (www.gitbook.com/book/nlesc/summerinthecity/details).

The third step, the UFS forecast, is the application of the system that was developed in steps 1 and 2 to produce finescale weather forecasts for the Amsterdam metropolitan region. This step includes the initialization of the model and the actual launch

of the UFS. Atmospheric fields are directly initialized from fields generated for the National Centers for Environmental Prediction (NCEP) Global Forecast System (GFS) cycle at 0000 UTC on a specific day (see www.nco.ncep.noaa.gov/pmb/products/gfs). These are available at a horizontal resolution of 0.25° × 0.25°. To initialize the land surface prognostic variables, fields of these variables are cycled from the UFS forecast of the previous day. Inland water temperatures and sea surface temperatures are initialized by interpolation of the average values of the locally observed water temperatures to the respective UFS grid points. The coarsest domain covers northwestern Europe, implying that at the outer boundaries, lateral boundary conditions (LBCs) need to be prescribed. For each daily forecast, the LBCs are updated every 6 h from the NCEP GFS forecast. More details about the initialization and the prescription of the LBCs are provided in the supplemental material.

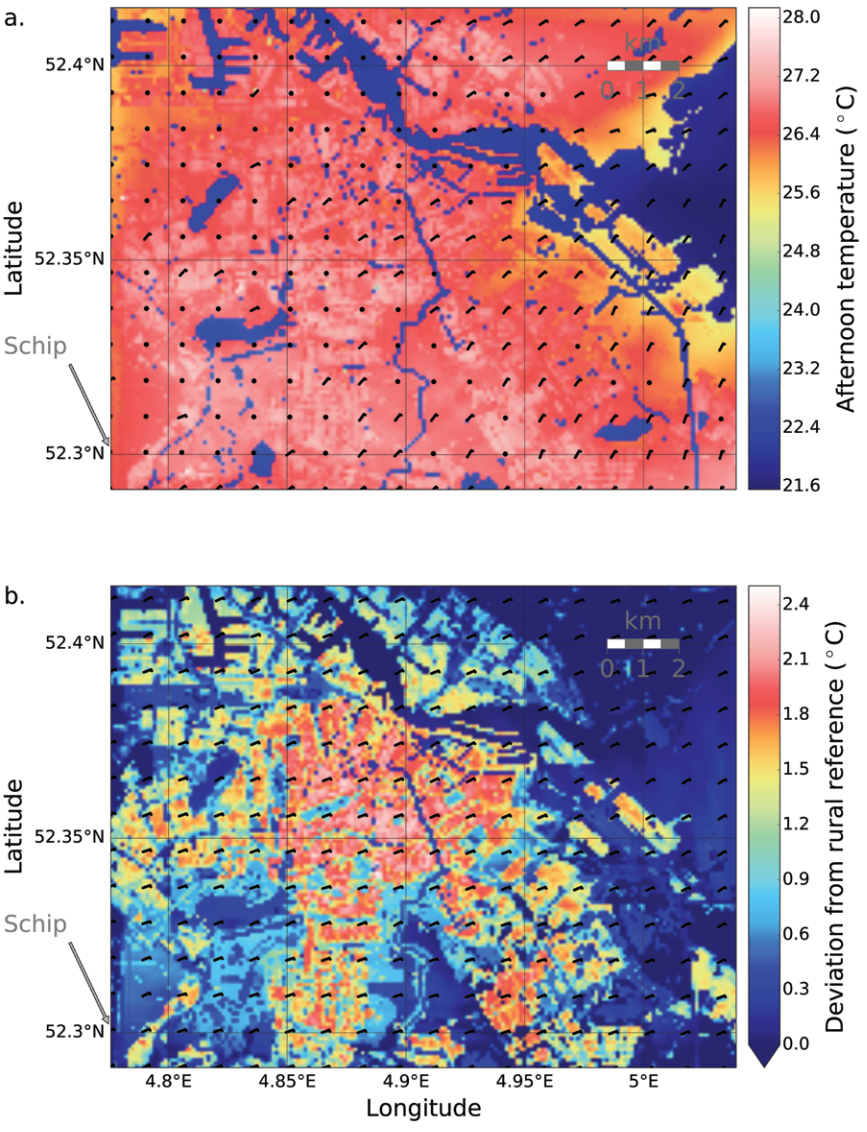

Fig. 4. UFS forecasts weather conditions with remarkable, unprecedented detail. (a) Forecast average afternoon (forecast hours 12, 13, 14, 36, 37, and 38) near-surface temperature (colored contours) and wind speed (wind barbs). (b) Forecast average evening (forecast hours 20, 21, 22, 44, 45, and 46) deviation of the local near-surface air temperature from that at Schiphol Airport and average evening wind speed. Forecasts are averaged over all forecasts produced during the warm weather episode from 29 June to 2 July 2015. Also indicated is the location of the Schiphol rural reference weather station.

When considering land use for the finest domain (Fig. 3a), the horseshoe-shaped historical city center (CC) of Amsterdam (old inner city and canal belt) is clearly visible, with suburbs extending to the west, south, southeast, and north of the water body (IJ). Parks appear as green spaces in urbanized areas. Landscapes in the rural areas around Amsterdam are characterized in part by the lake (IJmeer) in the east; grasslands in the south, southeast, and north; and a forest [Amsterdamse Bos (AB)], airport buildings, runways, and grasslands of Amsterdam's Schiphol Airport (SA) in the southwest (Fig. 3).

Both the impervious fraction of the surface and the aspect ratio vary considerably within the Amsterdam metropolitan region. The impervious fraction of the surface refers to the fraction of the surface that is covered by topographic elements that are impermeable to water (Fig. 3b). The aspect ratio (Fig. 3c) is defined as the ratio of the building height to the average width of the canyon. In general, both the impervious fraction and the aspect ratio are higher in the urbanized core of Amsterdam and lower in the western and eastern suburbs.

UFS FORECASTS FOR A WARM WEATHER EPISODE. Figure 4 shows that the UFS facilitates weather forecasting with unprecedented detail on the smallest (finest) forecast domain. Averaged over all forecasts produced during a warm weather episode from 29 June through 2 July 2015, the average afternoon (forecast hours 12, 13, 14, 36, 37, and 38) near-surface air temperature takes on its lowest value of about 21°C above the large water bodies (Fig. 4a). Highest temperature of about 28°C was forecasted for the southern and western suburbs of Amsterdam, which are relatively open areas with canyon widths that are relatively large as compared to the height of the surrounding buildings (Erell and Williamson 2007). The eastern suburbs of Amsterdam are considerably cooler because northeasterly winds bring in cool air from the eastern lake. Other (smaller) water bodies have a less drastic effect on air temperatures: the radii of influence vary from a hundred to a few hundred meters depending on the size of the water body.

Figure 4b shows the forecasted average evening (forecast hours 20, 21, 22, 44, 45, and 46) deviation of the local near-surface air temperatures as derived from the temperature forecast on the computational domain with a grid spacing of 500 m for Schiphol Airport (see location on Fig. 4b) produced during the warm weather episode. Taking Schiphol Airport to be a rural reference site, this deviation for urban areas is equivalent to the "canopy-layer UHI" (CLUHI) (Oke 1982), which is a concept that has been frequently used to quantify the effect of urban landscapes on local climate (e.g., Steeneveld et al. 2011; Smoliak et al. 2015). The highest values for CLUHI, amounting to about 2.5°C, were forecasted for the areas located west and south of the inner city of Amsterdam. For these areas, the fraction of the surface that is impervious is relatively high, and the aspect ratio is around one. Note that a value of one is the value for the aspect ratio at which it is known that the maximum (evening) UHI is maximal under Dutch summer conditions (Theeuwes et al. 2014). Low values for CLUHI were forecast for the water bodies, the city parks (CPs), and (to a lesser extent) the urbanized neighborhoods with a relatively low impervious fraction (Heusinkveld et al. 2014; Zipper et al. 2016).

AMSTERDAM OBSERVATIONAL NETWORK. We verified the UFS forecasts produced during JJA 2015 using the different forecasting domains against observations taken at the surface synoptic observation (SYNOP) weather station at Schiphol Airport and at 24 urban weather stations attached to lampposts at a height of 4 m throughout Amsterdam (see Fig. 1 and Table ES2). The observational network is with respect to observational density, observational techniques, and observational heights similar to the coarse array automatic weather station network that was installed in Birmingham, United Kingdom (Warren et al. 2016). According to the classification by Muller et al. (2013), the Amsterdam observational network should be characterized as a city-scale network. However, it can be argued that the observations are representative of the neighborhood scale. Recent studies carried out by Steeneveld et al. (2011), Heusinkveld et al. (2014), and Theeuwes et al. (2017) showed that for similar observational networks in Dutch towns, observations of the UHI could be related to urban characteristics such as population density and green fraction on a scale of a few hundred meters. Moreover, the observational network covers the entire range of Amsterdam neighborhoods: the historical center characterized by three-story warehouses along canals and small streets, the large neighborhoods surrounding the historical center that consist of three-story to four-story residential buildings dating from 1920 to 1940, the outer rim of Amsterdam characterized by relatively new neighborhoods with well-insulated three-story houses, and a small commercial strip in the southern part of Amsterdam with relatively high buildings and narrow street canyons.

The urban weather stations measure air temperature and humidity and consist of Decagon VP-3 humidity–temperature sensors, which are embodied in a round 184-mm-diameter shield. On top of the shield, a solar-powered aspiration fan (Davis) is installed, which is powered by two solar panels that are positioned above the shield at a ±45°angle to the east and west. To avoid temperature interference from the lampposts (Watkins et al. 2002), the shield and solar panels were attached to a 550-mm arm. The center of the shield is positioned 460 mm from the lamppost. Six of the urban stations were equipped with a DS-2 sonic anemometer from Decagon Devices. This sensor has a wind speed threshold of 0.00 m s^{-1} and a very high resolution of 0.01 m s^{-1}. Data on wind speed and direction are reported every 5 min. Wind speed data are available for Ams8, which is located on a small island east of Amsterdam; Ams3 and Ams6, which are located in suburban street canyons; Ams2 and Ams16, which are located in busy street canyons in the center of Amsterdam; and Ams25, which is located in a commercial area with relatively tall buildings.

Averaged 5-min data are stored on a ECMH20 datalogger (Decagon) and uploaded to the manufactures' website six times a day using a general packet radio service (GPRS) network.

As a rural reference, observations taken at Schiphol Airport were used. This weather station is a

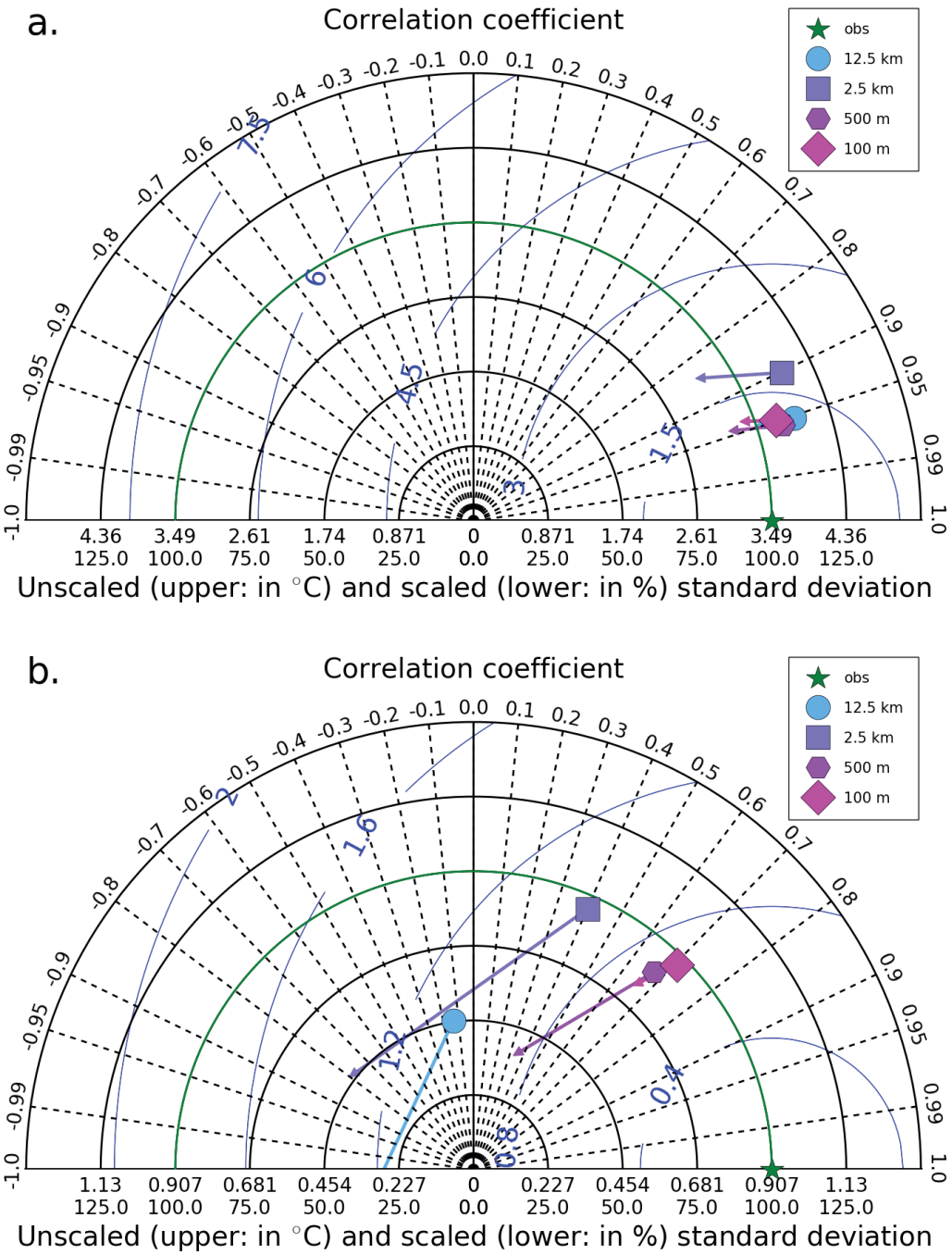

FIG. 5. Verifying the UFS forecasts produced during the summer of 2015. Taylor diagrams presenting the standard deviation (distance from origin) for the observations (obs) and the forecasts on the different (nested) forecast domains (see legend). The Pearson correlation coefficient between any forecast and the observations is given by the azimuthal scale; the centered root-mean-square error of any forecast is given by the distance between the forecast point and the observation point and is thus indicated by the blue contours. The mean bias (forecast minus observation) for any forecast is indicated by the arrows. The length of the arrow gives the magnitude of the bias. The direction of the arrow indicates the sign of the bias: when it is pointing to the right, as seen from the observation point, the mean bias is positive, while the mean bias is negative when the arrow points to the left. (a) The average afternoon near-surface temperature (No. of obs: 2,300). (b) The average evening CLUHI (No. of obs: 2,208). Note that the mean bias in CLUHI for the forecast on the domain with grid spacing of 12.5 km has such magnitude (1.3°C) that part of the arrow falls outside the Taylor diagram presented in (b).

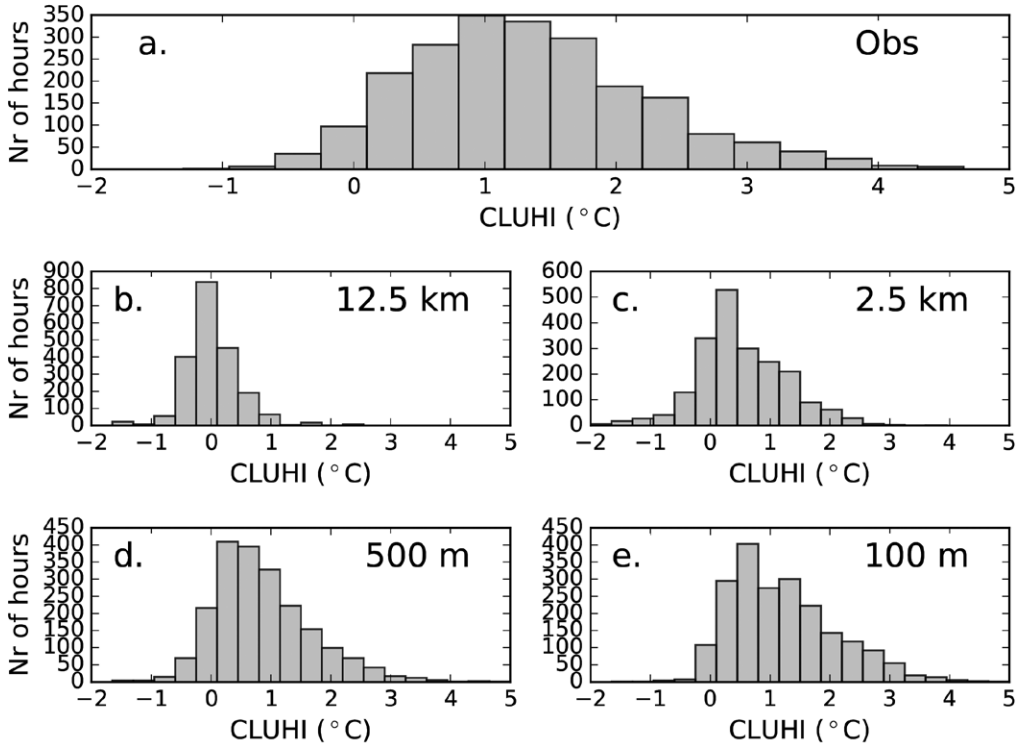

Fig. 6. Verifying the UFS forecasts produced during the summer of 2015. Histograms of the average evening CLUHI (No. of obs: 2,208) as derived from (a) the observations and the forecasts on the computational grids with grid sizes of (b) 12.5 km, (c) 2.5 km, (d) 500 m, and (e) 100 m.

SYNOP weather station [World Meteorological Organization (WMO) identifier 06240] and is located at 52.3010°N, 4.7740°E (see Fig. 1 for its location). As a SYNOP weather station, both the instrumental setup and the specification of the observational site are such that observations are achieved according to the regulations set out by the WMO. Available measurements include observations of the temperature, the dewpoint temperature, and the wind speed at a height of 1.5 m above the surface for a relatively open area in which surroundings are characterized by grassland and agricultural areas.

Data from the urban weather stations and the rural reference station were all binned into hourly averages.

VERIFYING THE URBAN FORECASTING SYSTEM. Figure 5 provides Taylor diagrams (Taylor 2001) displaying aggregated statistics for the average afternoon temperature and the average evening CLUHI using observations from all weather stations. For each location, aggregated statistics were calculated by contrasting hourly averages of forecast weather variables (see the supplemental material) directly with hourly averages of observed variables. We found that forecasts of the near-surface afternoon temperatures are very good (Fig. 5a): Pearson correlation coefficients r between forecasts and observations are all greater than 0.88, while forecast biases and values for the unbiased root-mean-square error (rmseu) are small. When forecasting the evening CLUHI, we found that refining the grid spacing clearly added skill to the weather forecast (Fig. 5b): the values for r on the domains with a grid spacing of 500 and 100 m were both around 0.7, while the values for the rmseu were around 1.0 K. The values for r for these grids were thus considerably higher than the values of approximately 0.4 for the domain with a grid spacing of 2.5 km and of approximately –0.14 for the domain with a grid spacing of 12.5 km. Although the values for r and the values for the rmseu for forecasts on the domains with grid spacing of 100 and 500 m are comparable, forecasts on 100 m had a smaller bias: –0.08° versus –0.43°C. The better performance of the forecasts on finer grids also becomes evident in Fig. 6, which shows histograms of the evening CLUHI for both the observations and the forecasts on the different computational domains. The histogram for the grid with a grid size of 12.5 km is narrow: most values for the CLUHI clustered around zero, which implies that forecasts at a resolution of

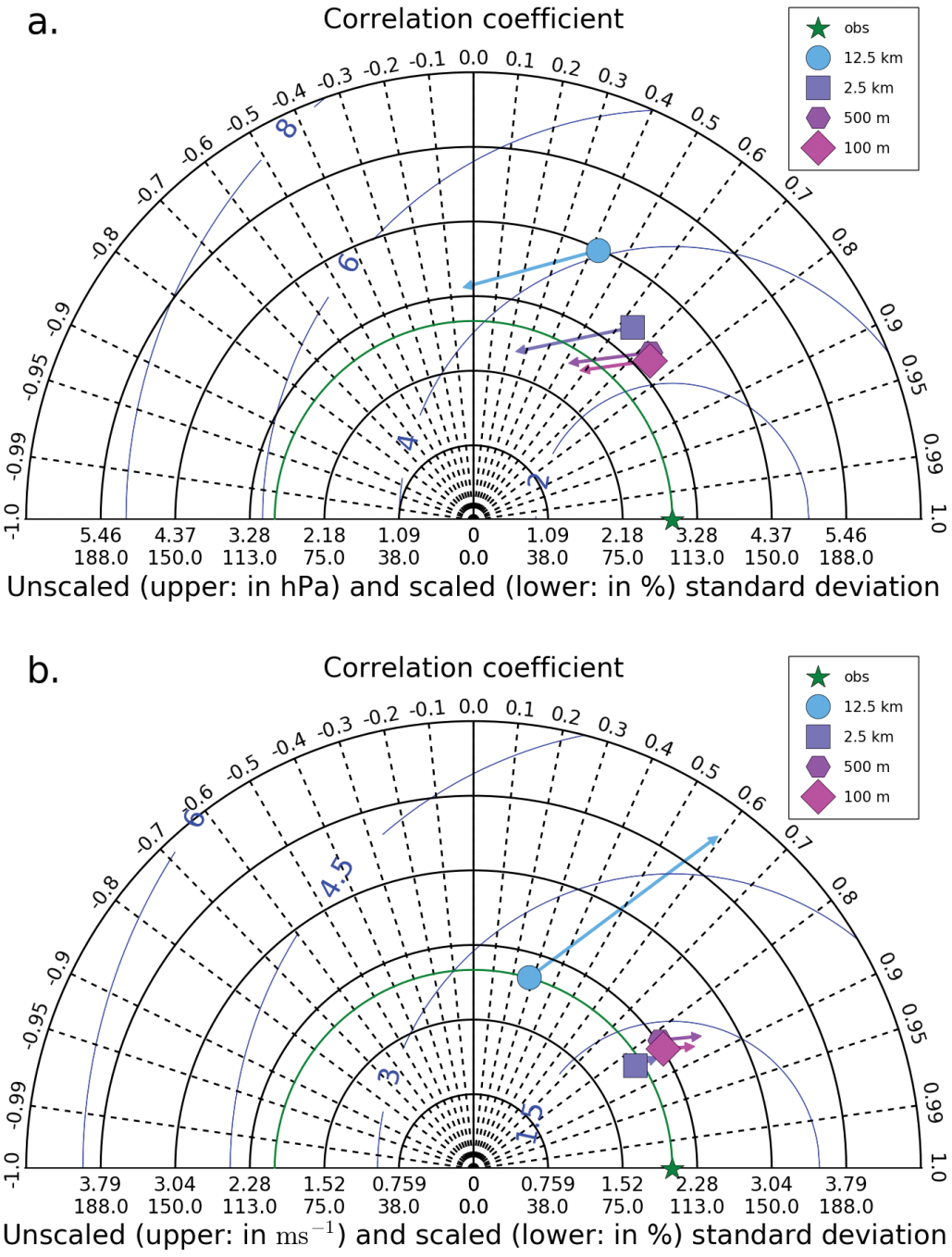

Fig. 7. Verifying the UFS forecasts produced during the summer of 2015. Taylor diagrams (see legend of Fig. 5 for explanation) of hourly averaged (all hours) (a) water vapor pressure (No. of obs: 110,400) and (b) wind speed (No. of obs: 30,912).

12.5 km hardly forecast urban evening temperatures that are higher than their rural counterparts. Forecasts on the refined computation domains are (much) better, particularly for the computational domains with grid sizes of 500 and 100 m. Forecasts on these computational domains yield histograms for the CLUHI that resemble the histogram based on the observations, though they tend to underestimate the CLUHI in conditions where the CLUHI is particularly strong.

Weather forecasting at a high resolution also improved forecasts for humidity (Fig. 7a): Pearson correlation coefficients for the forecasts on the

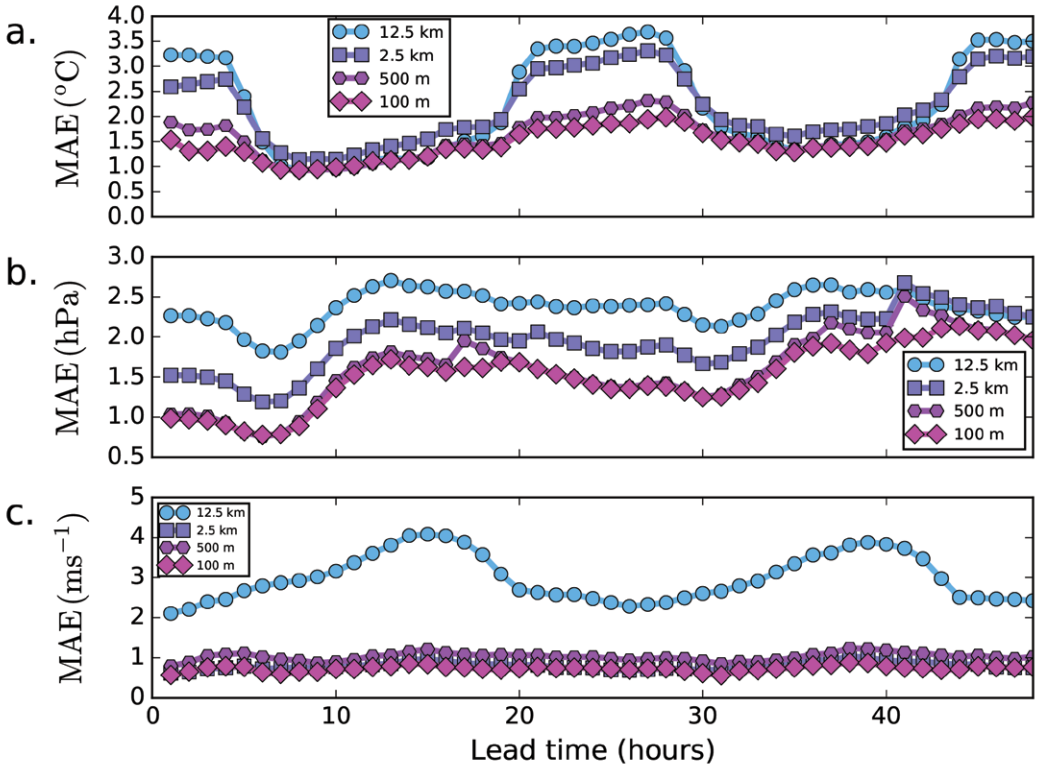

Fig. 8. Verifying the UFS forecasts produced during the summer of 2015. The MAE as a function of lead time for the (a) near-surface temperature, (b) near-surface water vapor pressure, and (c) near-surface wind speed for the forecasts on the different (nested) forecast domains (see legends).

domains with a grid spacing of 500 and 100 m were considerably higher than those for the forecasts on the domains with a grid spacing of 2.5 or 12.5 km. For wind speed (Fig. 7b), there was a clear distinction between the coarsest computational domain, which identifies the Amsterdam area as rural and thus has a tendency to overestimate the wind speed, and the finer computational grids that identify the Amsterdam area as urban and thus forecast lower, more realistic urban canyon wind speeds.

Figure 8 displays the median absolute error for all computational grids as a function of lead time for temperature (Fig. 8a), water vapor pressure (Fig. 8b), and wind speed (Fig. 8c). Overall, the forecast skill deteriorates with lead time: the median absolute error (MAE) at a lead time of 48 h was larger than the MAE at a lead time of 24 h for all forecasts. Furthermore, it appears that using fine resolutions of 500 and 100 m improved forecasts of weather variables during all times of the day, though the differences between fine-resolution (grid spacing of 500 and 100 m) forecasts and coarse-resolution (grid spacing of 12.5 and 2.5 km) forecasts were largest during the nighttime. For temperature and water vapor, forecast skill on a computation grid of 100 m was similar to the forecast skill on 500 m, though forecast skill on 100 m produced slightly better temperature forecasts during the nighttime. Particularly noteworthy is the large discrepancy between the forecast and the observed wind speed for the computational grid with a grid spacing of 12.5 km. On this domain, no land surfaces were classified as urban, implying that the forecast wind speed was, in contrast to the observed wind speed, typical of wind speed conditions over rural areas. For the remaining computational grids, errors in the wind speed forecasts were similar, suggesting that for wind speed, it is important that the urban canyon effects on wind speed are taken into account.

As SLUCM does not give estimates of the wind direction within the canyon, no verification for the wind direction for the urban land points could be carried out. We verified wind direction for the Schiphol SYNOP station. However, since this station is a rural station, forecasts on all resolutions gave estimates of the wind direction and the associated error statistics that were very similar (not shown).

FORECASTS FOR HUMAN THERMAL COMFORT. The UFS enables forecasts aimed at improving human thermal comfort. These are

made by translating the UFS forecasts for screen-level temperature and humidity into forecasts of the simplified wet-bulb globe temperature (SWBGT) (Fischer et al. 2012). The SWBGT is calculated as a linear combination of the screen-level temperature and water vapor pressure and can be considered as a proxy for the effectiveness of human thermal stress mitigation strategy using weather variables that are operationally readily available. Table 2 shows a contingency table (Wilks 2011) of the UFS forecasts on the finest computational domain for forecasting events occurring at the locations of the weather stations. During an afternoon hour, SWBGT exceeds 26°C, which is a threshold value associated with a moderate risk. It appears that the UFS is able to forecast such events of extreme heat. For instance, the hit rate (probability of detection) of the UFS amounts to 0.79, its false-alarm rate (probability of false detection) amounts to 0.015, and its critical success index amounts to 0.68.

Table 2. Contingency table for events when the afternoon SWBGT exceeds 26°C.

		Observed		
		Yes	**No**	**Total**
Forecast	**Yes**	853	179	1,032
	No	224	11,667	11,846
	Total	1,077	11,891	12,923

DISCUSSION AND CONCLUSIONS.

Extending traditional regional NWP, we developed a finescale weather forecasting system particularly designed for urban areas. The UFS consists of a full-fledged forecasting system that produces deterministic forecasts of relevant weather variables on a neighborhood level. The UFS was developed following the same principles used to build an operational weather forecasting system for the regional scale. However, in the current implementation of the UFS, the atmospheric fields are directly initialized using the global atmospheric model without any optimization of initial conditions by means of assimilation of local data (see Fig. 2).

The steps for development of the UFS are summarized in Fig. 2 and include the preparation of (geographical) datasets and the modification of the forecasting model such that it can be used to produce forecasts at the appropriate spatial scale for a Dutch summer period. At the actual launch of the forecast, the initial conditions and the boundary conditions from a global weather forecasting model need to be specified.

We applied our forecasting to produce a 48-h forecast of Dutch summer conditions. Driven by extensive land surface information, the UFS produces weather forecasts that forecast the spatial distribution of weather variables at a scale of a few hundred meters. The UFS appears to be able to take into consideration the impact of urban morphological characteristics and urban spatial structure on local temperatures (see Fig. 4) while it enables forecasts of human thermal comfort indices (Table 2) and assesses the increased electricity consumption during heat waves (not shown). Because these forecasts apply directly to scales on which people consume, sleep, work, and recreate, they can be used by the general public and governmental organizations in order to determine appropriate actions to take.

An obvious next step in the development of the UFS would be to extend the current deterministic forecast (Fig. 2) to an ensemble forecast in which the ensemble members differ with respect to applied model equations, (urban) physical parameterization, parameter values for the physical parameterization, and urban land surface characterization. This approach would allow for the quantification of the uncertainty of the forecast weather variables while also enabling the high-resolution forecasts that are calibrated using statistical calibration techniques such as the ensemble model output statistics technique (Gneiting et al. 2005) or the Bayesian model averaging technique (Raftery et al. 2005).

Another obvious improvement would be to replace the Smagorinsky first-order closure (3D) by a more detailed scheme since this method has some noted problems, such as an underrepresentation of horizontal scalar fluxes (Wyngaard 2004). This issue becomes particularly important when the UFS is applied in urbanized regions where horizontal gradients in mean variables are weak. In the Amsterdam region, horizontal gradients in mean variables are typically strong because of the large differences in land use (lakes, rural areas, and urban areas). Furthermore, use of the Smagorinsky first-order closure (3D) probably needs to be reconsidered when the vertical layering close to the surface is refined in such a way that fluxes in the surface layer are resolved by the atmospheric part of the weather forecast model. Also, recent literature (e.g., Mirocha et al. 2013) shows that the use of the Smagorinsky first-order closure (3D) leads to errors in wind speed calculations, especially in areas that are close to a boundary where air enters the domain. Obviously, this effect explains some of the discrepancies that we found between the observed

and forecasted wind speeds. However, as shown in Figs. 7b and 8c, the discrepancy between observed and forecasted wind speeds for the computational domains with grid sizes of 2.5 km and 500 and 100 m are similar despite the fact that on these grids, different formulations for turbulent fluxes within PBL are applied. This suggests that the effects of the formulations of turbulent fluxes are minor as compared to the differences in the formulations for other processes or the differences in the specification of the land surface characteristics or the initialization of the model (see also Talbot et al. 2012).

Another possible next step would be to extend the forecasts made by the UFS to other seasons. Care should then be taken when forecasting winter conditions since the observed fluxes of sensible heat (e.g., Ward et al. 2014) can be directed toward the surface during a significant part of the day, implying that during these months, PBL stratification might become such that the explicit assumption that the largest eddies are resolved on the finest computational grid is overstretched (Holtslag et al. 2013; Barlow 2014). It can be argued that under these conditions, all vertical turbulent fluxes become subgrid and need to be parameterized by selecting an appropriate PBL scheme. An obvious step forward would then be to include a so-called seamless turbulence scheme in WRF that blends the turbulence for a situation in which most turbulence fluxes are resolved on a scale of 100 m, with a situation where turbulent fluxes are parameterized using a one-dimensional PBL turbulence scheme (Boutle et al. 2014). Note that a similar solution might be beneficial to the intermediate computational domain where a grid spacing of 500 m is within the "terra incognita" of turbulence modeling (Wyngaard 2004). Another issue that needs to be addressed within the WRF adaptation step (see Fig. 2) is when one wishes to use the UFS for winter conditions. The aim would be to incorporate high-resolution inventories of the heat released by anthropogenic activities, which are an important source of energy in the atmospheric layers closest to the surface, particularly in winter (Bohnenstengel et al. 2014; Barlow 2014).

Application of the formulation of the UFS is not limited to relatively small cities such as Amsterdam. The proposed methodology can be used in other cities, including those in the United States and non-U.S. megacities. Since results will depend on specific situations and urban geometry, it is obvious that successful application of the UFS in other cities depends on the availability of (land surface) input and the verification of data resources as well as the availability of sufficient computing resources to perform calculations for the large areas that megacities occupy. Our results support the fact that NWP has made the next important step in its "quiet revolution" and has finally gone urban.

ACKNOWLEDGMENTS. This research was performed within the project entitled "Summer in the City—Forecasting and mapping thermal human comfort in urban areas," which was supported by the Netherlands eScience Center (ESOCCS 027.012.103). We thank the municipality of Amsterdam for allowing the installation of measurement devices on Amsterdam lampposts. We would also like to thank the Royal Netherlands Meteorological Institute for providing the data from the Schiphol Airport measurement station. A special thanks to Remko Uijlenhoet (Wageningen University) for his useful suggestions while preparing the manuscript. This work was carried out on the Dutch national e-infrastructure with the support of the SURF Cooperative under project SH-312-15.

REFERENCES

Barlow, J. F., 2014: Progress in observing and modelling the urban boundary layer. *Urban Climate*, **10**, 216–240, https://doi.org/10.1016/j.uclim.2014.03.011.

Bauer, P., A. Thorpe, and G. Brunet, 2015: The quiet revolution of numerical weather prediction. *Nature*, **525**, 47–51, https://doi.org/10.1038/nature14956.

Bohnenstengel, S. I., I. Hamilton, M. Davies, and S. E. Belcher, 2014: Impact of anthropogenic heat emissions on London's temperatures. *Quart. J. Roy. Meteor. Soc.*, **140**, 687–698, https://doi.org/10.1002/qj.2144.

Boutle, I. A., J. E. J. Eyre, and A. P. Lock, 2014: Seamless stratocumulus simulation across the turbulent gray zone. *Mon. Wea. Rev.*, **142**, 1655–1668, https://doi.org/10.1175/MWR-D-13-00229.1.

Chen, F., and Coauthors, 2011: The integrated WRF/urban modelling system: Development, evaluation, and applications to urban environmental problems. *Int. J. Climatol.*, **31**, 273–288, https://doi.org/10.1002/joc.2158.

Ching, J., and Coauthors, 2009: National Urban Database and Access Portal Tool. *Bull. Amer. Meteor. Soc.*, **90**, 1157–1168, https://doi.org/10.1175/2009BAMS2675.1.

Curriero, F. C., K. S. Heiner, J. M. Samet, S. L. Zeger, L. Strug, and J. A. Patz, 2002: Temperature and mortality in 11 cities of the eastern United States. *Amer. J. Epidemiol.*, **155**, 80–87, https://doi.org/10.1093/aje/155.1.80.

Erell, E., and T. Williamson, 2007: Intra-urban differences in canopy layer air temperature at a mid-latitude

city. *Int. J. Climatol.*, **27**, 1243–1255, https://doi.org/10.1002/joc.1469.

Fazeli, R., M. Ruth, and B. Davidsdottir, 2016: Temperature response functions for residential energy demand—A review of models. *Urban Climate*, **15**, 45–69, https://doi.org/10.1016/j.uclim.2016.01.001.

Fischer, E. M., K. W. Oleson, and D. M. Lawrence, 2012: Contrasting urban and rural heat stress responses to climate change. *Geophys. Res. Lett.*, **39**, L03705, https://doi.org/10.1029/2011GL050576.

Gneiting, T., A. E. Raftery, A. H. Westveld III, and T. Goldman, 2005: Calibrated probabilistic forecasting using ensemble model output statistics and minimum CRPS estimation. *Mon. Wea. Rev.*, **133**, 1098–1118, https://doi.org/10.1175/MWR2904.1.

Heusinkveld, B. G., G. J. Steeneveld, L. W. A. van Hove, C. M. J. Jacobs, and A. A. M. Holtslag, 2014: Spatial variability of the Rotterdam urban heat islands as influenced by urban land use. *J. Geophys. Res. Atmos.*, **119**, 677–692, https://doi.org/10.1002/2012JD019399.

Holtslag, A. A. M., and Coauthors, 2013: Stable atmospheric boundary layers and diurnal cycles: Challenges for weather and climate models. *Bull. Amer. Meteor. Soc.*, **94**, 1691–1706, https://doi.org/10.1175/BAMS-D-11-00187.1.

Hong, S.-Y., S. Y. Noh, and J. Dudhia, 2006: A new vertical diffusion package with an explicit treatment of entrainment processes. *Mon. Wea. Rev.*, **134**, 2318–2341, https://doi.org/10.1175/MWR3199.1.

Howard, L., 1833: *The Climate of London, Deduced from Meteorological Observations, Made in the Metropolis, and at Various Places around It*. Vol. 1, 2nd ed. Harvey and Darton, 338 pp.

Huynen, M. M., P. Martens, D. Schram, M. P. Weijenberg, and A. E. Kunst, 2001: The impact of heat waves and cold spells on mortality rates in the Dutch population. *Environ. Health Perspect.*, **109**, 463–470, https://doi.org/10.1289/ehp.01109463.

IPCC, 2013: *Climate Change 2013: The Physical Science Basis*. Cambridge University Press, 1535 pp., https://doi.org/10.1017/CBO9781107415324.

Kovats, S., and G. Bickler, 2012: Health protection and heatwaves: The need for systematic review. *Cochrane Database Syst. Rev.*, **2012** (7), https://doi.org/10.1002/14651858.ED000044.

Kusaka, H., H. Kondao, Y. Kikegawa, and F. Kimura, 2001: A simple single-layer urban canopy model for atmospheric models: Comparison with multi-layer and slab models. *Bound.-Layer Meteor.*, **101**, 329–358, https://doi.org/10.1023/A:1019207923078.

McGregor, R., Ed., 2015: Heatwaves and health: Guidance on warning-system development. World Meteorological Organization–World Health Organization Rep. WMO-1142, 114 pp., www.who.int/globalchange/publications/WMO_WHO_Heat_Health_Guidance_2015.pdf?ua=1.

Mirocha, J., G. Kirkil, E. Bou-Zeid, F. Katopodes Chow, and B. Kosovic, 2013: Transition and equilibration of neutral atmospheric boundary layer flow in one-way nested large-eddy simulations using the Weather Research and Forecasting Model. *Mon. Wea. Rev.*, **141**, 918–940, https://doi.org/10.1175/MWR-D-11-00263.1.

Muller, C. L., L. Chapman, C. S. B. Grimmond, D. T. Young, and C. Xai, 2013: Sensors and the city: A review of urban meteorological networks. *Int. J. Climatol.*, **33**, 1585–1600, https://doi.org/10.1002/joc.3678.

Narita, K., 2007: Experimental study of the transfer velocity for urban surfaces with a water evaporation method. *Bound.-Layer Meteor.*, **122**, 293–320, https://doi.org/10.1007/s10546-006-9116-y.

Oke, T. R., 1982: The energetic basis of the urban heat island. *Quart. J. Roy. Meteor. Soc.*, **108**, 1–24, https://doi.org/10.1002/qj.49710845502.

Pappenberger, F., G. Jendritzky, H. Staiger, E. Dutra, F. Di Giuseppe, D. S. Richardson, and H. L. Cloke, 2015: Global forecasting of thermal health hazards: The skill of probabilistic predictions of the Universal Thermal Climate Index (UTCI). *Int. J. Biometeor.*, **59**, 311–323, https://doi.org/10.1007/s00484-014-0843-3.

Pirard, P., S. Vandentorren, M. Pascal, K. Laaidi, A. Le Tertre, S. Cassadou, and M. Ledrans, 2005: Summary of the mortality impact assessment of the 2003 heat wave in France. *Eurosurveillance*, **10**, 153–155.

Raftery, A. E., T. Gneiting, F. Balabdaoui, and M. Polakowski, 2005: Using Bayesian model averaging to calibrate forecast ensembles. *Mon. Wea. Rev.*, **133**, 1155–1174, https://doi.org/10.1175/MWR2906.1.

Rydin, Y., and Coauthors, 2012: Shaping cities for health: Complexity and the planning of urban environments in the 21st century. *Lancet*, **379**, 2079–2108, https://doi.org/10.1016/S0140-6736(12)60435-8.

Skamarock, W. C., and J. B. Klemp, 2008: A time-split nonhydrostatic atmospheric model for weather research and forecasting applications. *J. Comput. Phys.*, **227**, 3465–3485, https://doi.org/10.1016/j.jcp.2007.01.037.

Smoliak, B. V., P. K. Snyder, T. E. Twine, P. M. Mykleby, and W. F. Hertel, 2015: Dense network observations of the Twin Cities canopy-layer urban heat island. *J. Appl. Meteor. Climatol.*, **54**, 1899–1917, https://doi.org/10.1175/JAMC-D-14-0239.1.

Steeneveld, G. J., S. Koopmans, B. G. Heusinkveld, L. W. A. van Hove, and A. A. M. Holtslag, 2011: Quantifying urban heat island effects and human comfort for cities of variable size and urban morphology in the

Netherlands. *J. Geophys. Res.*, **116**, D20129, https://doi.org/10.1029/2011JD015988.

Talbot, C., E. Bou-Zeid, and J. Smith, 2012: Nested mesoscale large-eddy simulations with WRF: Performance in real test cases. *J. Hydrometeor.*, **13**, 1421–1441, https://doi.org/10.1175/JHM-D-11-048.1.

Taylor, K. E., 2001: Summarizing multiple aspects of model performance in a single diagram. *J. Geophys. Res.*, **106**, 7183–7192, https://doi.org/10.1029/2000JD900719.

Theeuwes, N. E., G. J. Steeneveld, R. J. Ronda, B. G. Heusinkveld, L. W. A. van Hove, and A. A. M. Holtslag, 2014: Seasonal dependence of the urban heat island on the street canyon aspect ratio. *Quart. J. Roy. Meteor. Soc.*, **140**, 2197–2210, https://doi.org/10.1002/qj.2289.

——, ——, ——, and A. A. M. Holtslag, 2017: A diagnostic equation for the daily maximum urban heat island effect for cities in northwestern Europe. *Int. J. Climatol.*, **37**, 443–454, https://doi.org/10.1002/joc.4717.

United Nations, 2014: World urbanization prospects: 2014 revision. United Nations Department of Economic and Social Affairs Rep. ST/ESA/SER.A/352, 32 pp., https://esa.un.org/unpd/wup/Publications/Files/WUP2014-Highlights.pdf.

U.S. Environmental Protection Agency, 2008: Reducing urban heat islands: Compendium of strategies. U.S. Environmental Protection Agency Rep., 177 pp., www.epa.gov/heat-islands/heat-island-compendium.

Ward, H. C., J. G. Evans, and C. S. B. Grimmond, 2014: Multi-scale sensible heat fluxes in the suburban environment from large-aperture scintillometry and eddy covariance. *Bound.-Layer Meteor.*, **152**, 65–89, https://doi.org/10.1007/s10546-014-9916-4.

Warren, E. L., D. T. Young, L. Chapman, C. Muller, C. S. B. Grimmond, and X.-M. Cai, 2016: The Birmingham Urban Climate Laboratory—A high density, urban meteorological dataset, from 2012–2014. *Sci. Data*, **3**, 160038, https://doi.org/10.1038/sdata.2016.38.

Watkins, R., J. Palmer, M. Kolokotroni, and P. Littlefai, 2002: The London heat island: Results from summertime monitoring. *Build. Serv. Eng. Res. Technol.*, **23**, 97–106, https://doi.org/10.1191/0143624402bt031oa.

Wilks, D. S., 2011: *Statistical Methods in the Atmospheric Sciences*. 3rd ed. Elsevier, 676 pp.

Wyngaard, J. C., 2004: Toward numerical modeling in the "terra incognita." *J. Atmos. Sci.*, **61**, 1816–1826, https://doi.org/10.1175/1520-0469(2004)061<1816:TNMITT>2.0.CO;2.

Zander, K. K., W. J. W. Botzen, E. Oppermann, T. Kjellstrom, and S. T. Garnett, 2015: Heat stress causes substantial labour productivity loss in Australia. *Nat. Climate Change*, **5**, 647–651, https://doi.org/10.1038/nclimate2623.

Zipper, S. C., J. Schatz, A. Singh, C. J. Kucharik, P. A. Townsend, and S. P. Loheide, 2016: Urban heat island impacts on plant phenology: Intra-urban variability and response to land cover. *Environ. Res. Lett.*, **11**, 054023, https://doi.org/10.1088/1748-9326/11/5/054023.